Electronic Supplementary Information

In-situ Formed Catalysts for Active, Durable, and Thermal-stable Ammonia Protonic Ceramic Fuel Cells at 550 °C

Hua Zhang[1], Kang Xu[1], Yangsen Xu[1], Fan He[1], Feng Zhu[1], Kotaro Sasaki[2], YongMan Choi[3*], and Yu Chen[1*]

[1]School of Environment and Energy, South China University of Technology, Guangzhou, 510006, China

[2]Chemistry Division, Brookhaven National Laboratory, Upton, NY 11973, USA

[3]College of Photonics, National Yang Ming Chiao Tung University, Tainan 71150, Taiwan

*Corresponding authors:

YongMan Choi (ymchoi@nycu.edu.tw);

Yu Chen (eschenyu@scut.edu.cn).

Materials and Methods

Fabrication of single cells

Shown in **Figure S1** is the single-cell fabrication process. The single cells were fabricated via robust processes of tape-casting, high-temperature co-sintering, and screen-printing. Typically, about 100 cells are fabricated in one batch. The anode-supported half-cells were lab-prepared via a three-layer tape-casting: the electrolyte layer, anode functional layer, and anode supporting layer were sequentially cast onto a polymer film, as shown in **Figure S1a-d**. After being sufficiently dried in ambient air at room temperature for ~15h, the green tape (before being fired) was punched into about 100 pellets with a diameter of ~15mm (**Figure S1e**) and pre-heated at 600°C for 2h (**Figure S1f**). A slow heating (a rate of 0.5 ^{o}C min^{-1}) was applied throughout the pre-heating procedure to eliminate all organic components from the pellets without cracking. After that, the pre-fired three-layered pellets (anode support layer, anode functional layer, and electrolyte) were co-sintered at 1450 ^{o}C for 5 h to create anode-supported half cells (**Figure S1g**). The $PrBa_{0.5}Sr_{0.5}Co_{1.5}Fe_{0.5}O_{5+\delta}$ (PBSCF) cathodes were then screen-printed onto the electrolyte of half cells. The full cells were then fired in the air at 950 °C for 2 h (with an active area of 0.2826 cm^2) (**Figure S1h**).

Fabrication of the symmetrical cells

Symmetric cells with a configuration of Ni/BZCYYb|BZCYYb|Ni/BZCYYb were fabricated by screen-printing Ni/BZCYYb anode pastes onto both sides of a BZCYYb pellet. To prepare dense BZCYYb pellets, the BZCYYb powder was first mixed with 1 wt% NiO and adequate ethanol, then ball-milled for 24 h, and followed pressed into a pellet after drying, finally sintering at 1450°C for 5 h. The NiO-BZCYYb powders were mechanically mixed with organic additives (α-terpineol and ethylcellulose) to form a Ni/BZCYYb anode slurry. Ni/BZCYYb anode slurry was then screen-printed on opposite sides of the BZCYYb pellet and subsequently sintered at 1450 °C for 5 h under an air atmosphere (with an area of 0.2826 cm^2), forming porous composite electrodes. The external Ag wires served as the current collectors were attached to the electrode with Ag conducting glue (Shanghai Research Institute of Synthetic resins) as the binder. Prior to the symmetrical cells test, the symmetrical anode cells were heated

to 700 °C in H_2 at a flow rate of 20 mL min^{-1} with a heating rate of 10 °C min^{-1} and followed by reduction at 700 °C for 30 min in H_2 at a flow rate of 20 mL min^{-1}. The symmetrical anode cells were then fed with NH_3 at a flow rate of 10 mL min^{-1}. The symmetrical anode cells were run at temperatures ranging from 700 °C to 550 °C. All impedance tests had a frequency range of 100 mHz to 10 kHz and an AC amplitude of 10 mV.

Catalyst Preparation

Stoichiometric amounts of high-purity $Cu(NO_3)_2 \cdot 3H_2O$, and $Ru(NO)(NO_3)_x(OH)_y$, x+y=3 were dissolved in DI water to form 0.1M Ru_xCu_{1-x} (x=0, 0.05, 0.25, 0.5, 0.75, 0.95, and 1) solution. A stoichiometric amount of citric acid was added as a complexing agent and fuel for subsequent self-combustion. 5 μL of the stock solution was deposited on the porous Ni/BZCYYb anode surface. The loading of the catalyst was increased by repeating the infiltration process. The coatings were fired at 700 °C for 2 h during the cell start-up stage.

Preparation of $PrBa_{0.5}Sr_{0.5}Co_{1.5}Fe_{0.5}O_{5+\delta}$（PBSCF）powder

A citric nitrate solution combustion process was used to provide $PrBa_{0.5}Sr_{0.5}Co_{1.5}Fe_{0.5}O_{5+\delta}$ (PBSCF) power. In DI water, stoichiometric amounts of $Pr(NO_3)_3$, $Ba(NO_3)_2$, $Sr(NO_3)_2$, $Co(NO_3)_2 \cdot 6H_2O$, and Fe $(NO_3)_3 \cdot 9H_2O$ were dissolved to form a solution of $PrBa_{0.5}Sr_{0.5}Co_{1.5}Fe_{0.5}O_{5+\&}$. As the complexing agent and fuel for later self-combustion, sieometric quantities of ctric acid (CA) and glycine were applied. CA: glycine ratio of 1:0.75:0.75. The power was then heated for 2 hours at 900 °C.

Catalytic test for Ru_xCu_{1-x}-Ni/BZCYYb powder

The catalytic activity of Ni/BZCYYb powder was carried out on a continuous fixed-bed quartz reactor (catalyst: 0.3 g, 10-15 mesh) under pure NH_3 with a flow rate of 10 mL min^{-1}. Firstly, the powder of Ni/BZCYYb catalysts was heated to 700°C in an H_2 flow (40 mL min^{-1}) with a heating rate of 5°C min^{-1} and followed by reducing at 700°C for 2 h in H_2 at a flow rate of 40 mL min^{-1}. Then, the gas was switched to NH_3 (10 mL min^{-1}) and the catalysts were heated in the range of 400-700°C. The measurement of effluent gas was introduced to a sulfuric acid aqueous solution to

remove unreacted ammonia and analyzed using on-line gas chromatograph (GC-7820, Shimadzu) equipped with a thermal conductivity cell detector (TCD). The conversion of ammonia was calculated by the following Eq. (4)

$$NH_3\ conversion = \left(1 - \frac{n_{NH_3 outlet}}{n_{NH_3 inlet}}\right) \times 100\% \quad (4)$$

where $n_{NH_3 outlet}$ and $n_{NH_3 outlet}$ are the molar ratio of outlet and inlet ammonia, respectively.

Electrochemical Measurements

The Ni-BZCYYb/BZCYYb/PBSCF single-cell was placed in the test rig's furnace. The electrode surface was partially linked with Ag mesh for electrochemical testing using Ag paste (DAD-87, acquired from Shanghai Synthetic Resin Research Institute). Prior to the electrochemical test, the single cell was heated to 700°C in ambient air, then the anode was reduced in 3% humidified H_2 (3% H_2O) at a flow rate of 30 mL min^{-1}, and the composite cathode was exposed to ambient air. The anode was then fed with NH_3 at a flow rate of 20 mL min^{-1}. The single cell was run at temperatures ranging from 550 °C to 700 °C.

The values of the open-circuit voltage (OCV), current-voltage (I-V), and impedance spectra of a single cell fueled with hydrogen and ammonia were measured using an electrochemical workstation (AMETEK PARSTAT MC). The cell was discharged at 0.2 A cm^{-2} at 550 °C for the long-term stability testing of the NH_3-fueled SOFC. All impedance tests had a frequency range of 100 mHz to 10 kHz and an AC amplitude of 10 mV.

Characterization

The microscopic morphology analysis of the cell was performed using a thermal field emission scanning electron microscope (SEM, Hitachi SU8010, Japan) or a transmission electron microscope equipped with energy-dispersive spectrum analysis (JEOL 4000EX). A standard cross-section sample preparation routine was followed for the preparation of the TEM samples. Specifically, bulk samples were cut into rectangle pieces (2.2 mm×1.5 mm) and then attached face-to-face together by the conductive

epoxy. Then the two sides of the samples were mechanically polished down to 100 μm, followed by dimpling to 20 μm. Then sample was transferred onto a Cu ring and ion milled to open a hole in the middle. The crystal structures of the as-synthesized Ni/BZCYYb and after 30μL of 0.1M Ru_xCu_{1-x} (x=0, 0.05, 0.25, 0.5, 0.75, 0.95, and 1) infiltration exposure at 700 °C for 2 h were measured by X-ray diffractometer (Rigaku, Miniflex model) with Cu Ka radiation at room temperature.

Computational methods

First-principles density functional theory (DFT) calculations were performed using the Vienna Ab Initio Simulation Package (VASP) [1, 2] to examine the boosted activity of ammonia decomposition using heterostructured $Ru_{0.95}Cu_{0.05}Ni_x$ (RCN) deposited on the Ni-BZCYYb anode. We applied the Perdew-Burke-Ernzeroh (PBE) exchange-correlation functional [3] with the projector augmented plane wave (PAW) method [4] and a kinetic energy cutoff of 415 eV. The Brillouin-zone integration was conducted with the Γ-centered (3 × 3 × 3) and (3 × 3 × 1) **k**-point mesh grids for the bulk modes. For surface calculations, a vacuum space of 15 Å in the z-direction was introduced, and the Γ-centered (3 × 3 × 1) ***k***-point mesh was employed with a Gaussian smearing method (σ = 0.05 eV) and dipole corrections. We constructed three-layer p(3 × 3) surfaces of Ni(111) (36 Ni atoms) and RuCuNi(111) (1 Ru, 1 Cu, and 34 Ni atoms). Two atomic layers of the surfaces at the bottom were fixed to the bulk properties. The climbing-image nudged elastic band (CI-NEB) method [5] was applied to locate transition states between an initial state (a reactant) and a final state (a product) after calculating adsorption energies (ΔE_{ads}) by E_{ads} = E(adsorbate/surface) – E(surface) – E(adsorbate), where E(adsorbate/surface) is the total energy of the adsorbate-bare surface, E(surface) is the total energy of the bare surface without adsorbates, and E(adsorbate) is the total energy of a gas-phase species. In this study, we neglected zero-point energy (ZPE) corrections.

Supplementary Note 1

In order to characterize the detailed electronic structure of the catalysts, we have employed X-ray photoelectron spectroscopy (XPS). The electronic states of the reduced RCN anode were characterized by high resolution XPS (**Figure S5a**). All the binding energy scales are calibrated using the C 1s peak with a binding energy of 284.8 eV. XPS survey spectra for the reduced RCN anode confirm the presence of Ni, O and C; however, peaks associated to Cu and Ru were undetectable due probably to their low loading (30μL (~3.0 mg cm^{-2})) (**Figure S5a**). In the high-resolution Ni $2p_{3/2}$ spectrum of the reduced RCN anode **Figure S5b**), three deconvolution peaks can be obtained. The peaks at 852.8 eV correspond to the Ni $2p_{3/2}$ of Ni metal, indicating the presence of Ni metal in the RCN anode. The peaks of Ni $2p_{3/2}$ at 855.7 eV in combination with the satellite peaks are the typical characteristics of Ni^{2+} [6].

To determine the possible reaction between the $Ru_{0.95}Cu_{0.05}$ catalyst and the Ni/BZCYYb anode under experimental conditions, the electronic structure of the reduced Ni/BZCYYb+$Ru_{0.95}Cu_{0.05}$ composite (mass ratio of 1:1) was tested, as shown in **Figure S5c-f**. XPS survey spectra confirm the presence of Ni, Cu, Ru, O and C, shown in (**Figure S5c**). Similarly, in the high-resolution Ni $2p_{3/2}$ spectrum of the reduced bare anode+$Ru_{0.95}Cu_{0.05}$ composite (**Figure S5d**), three deconvolution peaks can be obtained. The peaks at 852.8 eV correspond to the Ni $2p_{3/2}$ of Ni metal, indicating the presence of Ni metal in the RCN anode. The peaks of Ni $2p_{3/2}$ at 855.7 eV in combination with the satellite peaks are the typical characteristics of Ni^{2+}. The Cu $2p_{3/2}$ have two deconvolution peaks (**Figure S5e**). The peaks at 932.4 eV correspond to the Cu $2p_{3/2}$ of Cu metal, indicating the existence of metallic Cu. Meanwhile, the peaks of Cu 2p3/2 at 933.68 eV are the typical characteristics of Cu^{2+} [7, 8]. From the Ru 3p spectra (**Figure S5f**), the Ru $3p_{3/2}$ peaks at 460.3 eV confirm the presence of metallic Ru. Combined with the XPS and XRD results (**Figure 1d-e**, and **Figure S4**), Ni electronic structures have been changed with the incorporation of $Ru_{0.95}Cu_{0.05}$, and the metallic Ni and metallic Ru-Cu would react to form Ru-Cu-Ni alloy NPs. Since no any obvious Ni- or Cu-oxides are observed from the XRD patterns (**Figure 1d-e**), it is

suggested that the detected signals of Ni^{2+} and Cu^{2+} could be ascribed to the slightly oxidization shells on their surfaces [6, 7] .

Supplementary Note 2

In order to gain more insights into the detailed electrochemical process of the bare, Ru_xCu_{1-x}-Ni/BZCYYb (x=0.05, 0.25, 0.5, and 0.75) anodes, RCN, and $RuNi_x$ anodes in NH_3 at 550 °C, we have also analyzed the impedance spectra using distribution of relaxation time (DRT). As shown in **Figure S7,** three peaks were identified at high frequency (HF: 10^4-10^5 Hz), intermediate frequency (IF: 10^0-10^4 Hz), and low frequency (LF: 10^{-2}-10^0 Hz), corresponding to at least three distinct electrochemical processes [9]. The HF is most likely connected to the H^+ transport process in the electrode/electrolyte interface; the IF to NH_3 dissociative adsorption, decomposition, and H_2 dissociation process on anode surface [10, 11], whereas the LF is likely related to the gas diffusion process within the pores of the anode substrate [12, 13]. As shown in **Figure S7a**, the integral resistance of the HF and IF process decreased continuously with time when using the Ru-modified anode ($RuNi_x$) anode, indicating that Ru modification can accelerate the charge transfer (HF) and surface exchange process (IF), but has little effect on the LF. As shown in **Figure S7b**, the integral resistance of the HF and IF processes decreased continuously with time as Ru content increased from 0.05 to 0.5 in the Ru_xCu_{1-x}-Ni/BZCYYb (x=0.05, 0.25, 0.5, and 0.75) anodes, indicating that Ru can accelerate the charge transfer (HF) and surface exchange process (IF), but has a negative effect on the LF. However, using the RCN anode not only accelerates the two processes at HF and IF, but it also has a positive effect on the other mass transfer process (LF), demonstrating that the RCN anode has greater catalytic activity than the monometallic active phases due to surface electrical structure modification coupled with the optimized surface morphology [7].

Supplementary Figures

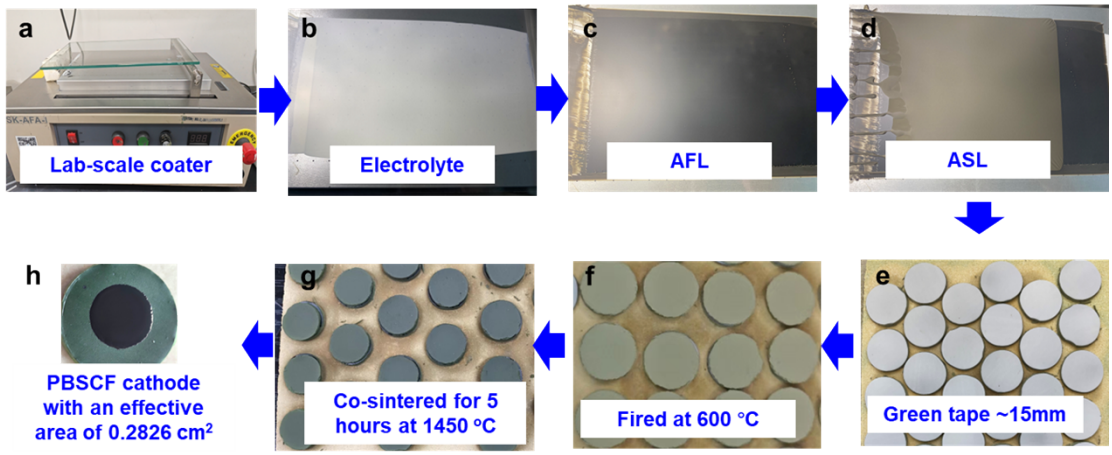

Figure S1. A demonstration of relatively single cells manufacturing by using tape casting and co-sintering process. (a) Photos of a lab-scale coater. The anode-supported half-cells with casting: (b) the electrolyte layer, (c) anode functional layer, and (d) anode supporting layer. (e) The green pellets (before firing) with a diameter of ~15mm. (f) The anode supported half cells after pre-heated at 600°C for 2h. (g) The anode supported half cells after sintering for 5 h at 1450 °C. (h) The full PCFC cell after sintering and applying the PBSCF cathode with an effective area of 0.2826 cm^2.

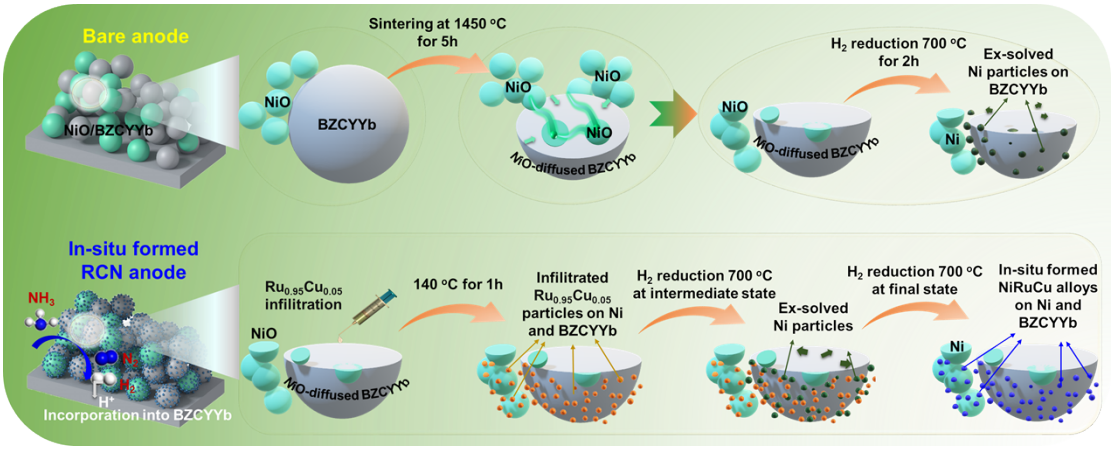

Figure S2. Schematics of the in-situ formation process between infiltrated $Ru_{0.95}Cu_{0.05}$ and exsolved Ni nanoparticles from the BZCYYb phase (from the anodes).

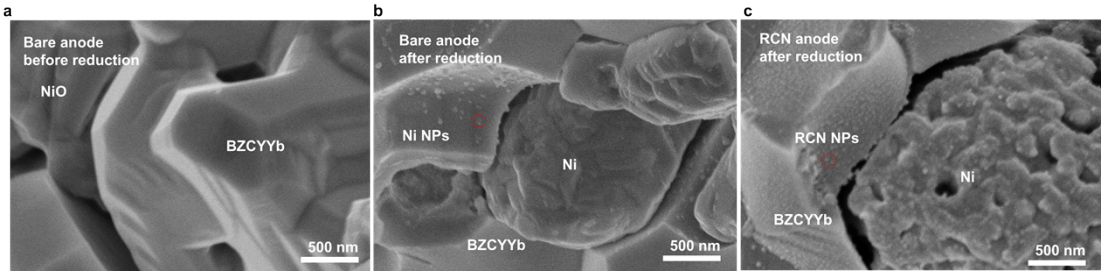

Figure S3. Typical SEM image of the (a) bare anode before reduction; (b) bare anode after reduction at 700 ^{o}C in wet H_2 for 2 h; and (c) RCN anode after reduction at 700 ^{o}C in H_2 for 2 h.

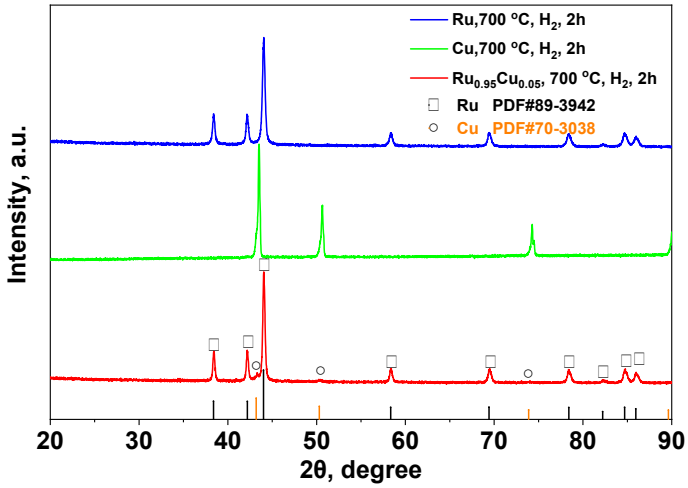

Figure S4. XRD patterns of the Ru, Cu and $Ru_{0.95}Cu_{0.05}$ catalysts after H_2 treatment at 700 °C for 2 h.

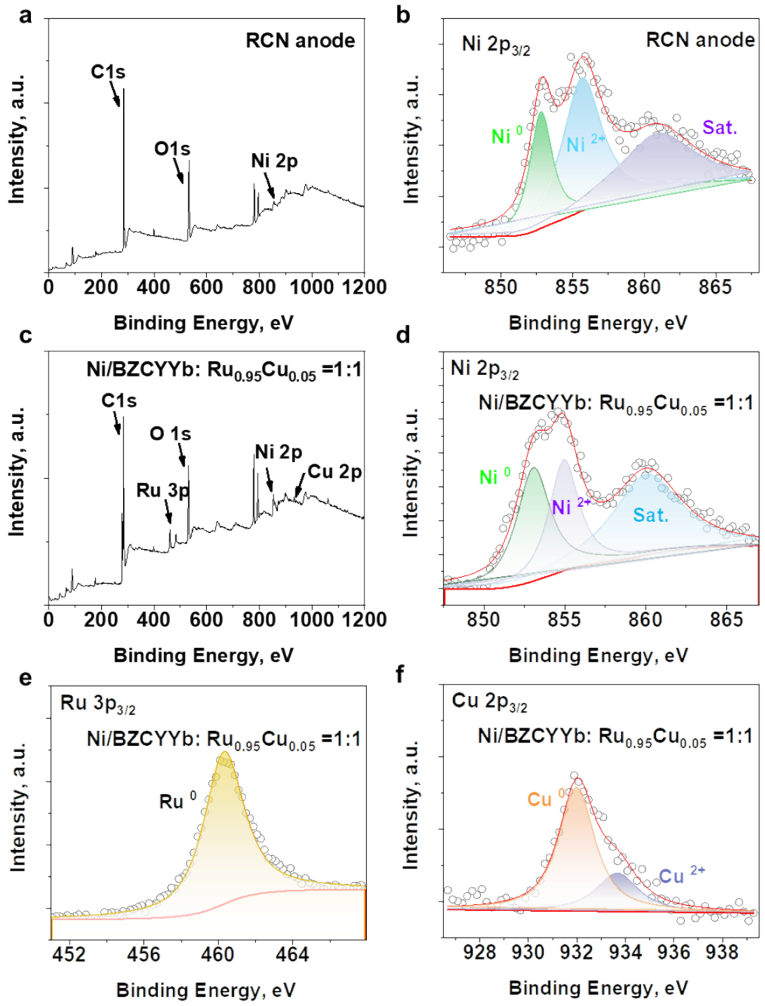

Figure S5. (a) XPS survey spectra, and (b) high-resolution Ni $2p_{3/2}$ of reduced RCN anode. (c) XPS survey spectra, and (d) high-resolution Ni $2p_{3/2}$, (e) Ru $3p_{3/2}$, and (f) Cu $2p_{3/2}$ of reduced Ni/BZCYYb+$Ru_{0.95}Cu_{0.05}$ composite (mass ratio of 1:1).

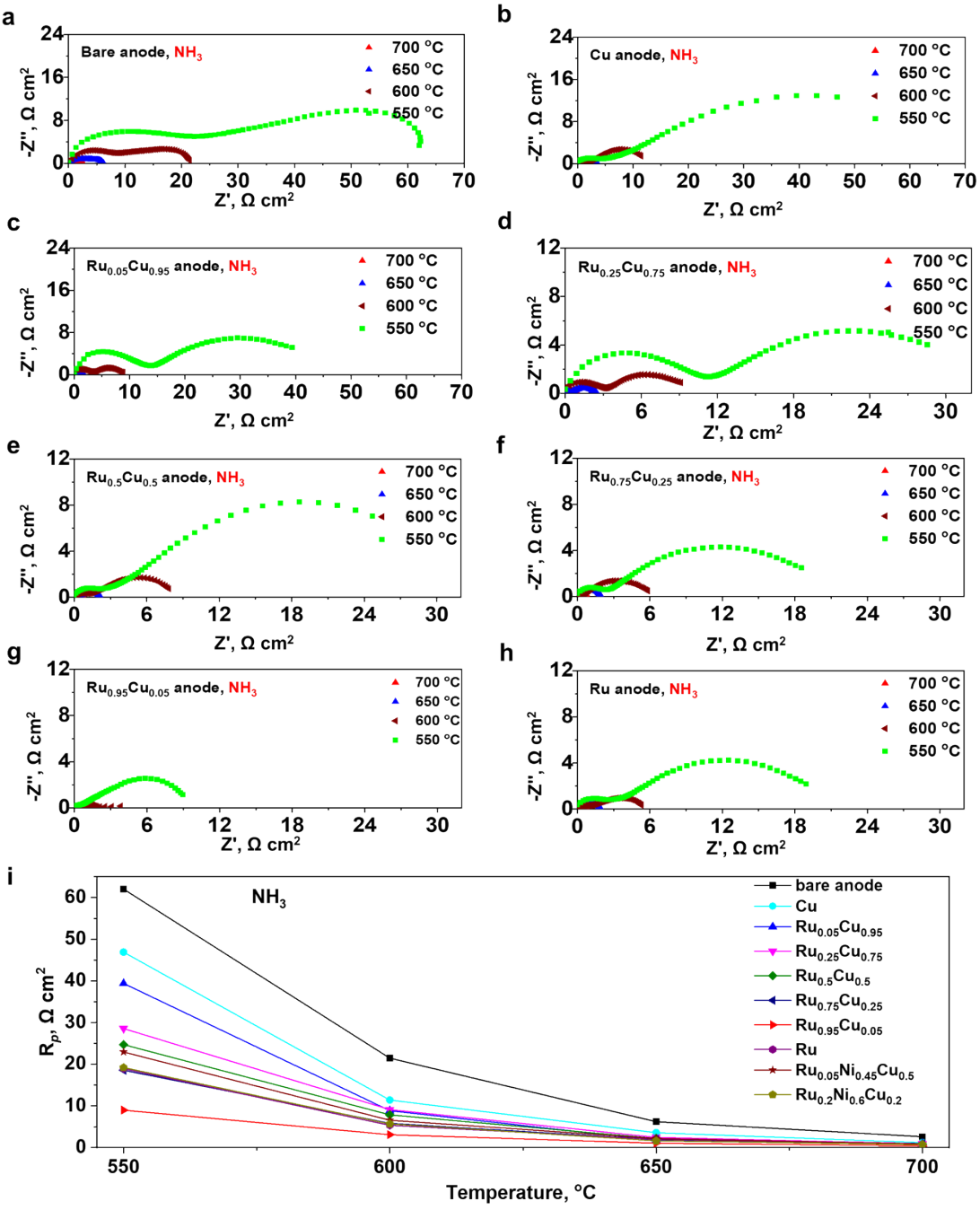

Figure S6. Electrochemical impedance spectra of the **(a)** bare Ni/BZCYYb anode, (b) Cu-Ni/BZCYYb anode, (c) $Ru_{0.05}Cu_{0.95}$-Ni/BZCYYb anode, (d) $Ru_{0.25}Cu_{0.75}$-Ni/BZCYYb anode, (e) $Ru_{0.5}Cu_{0.5}$-Ni/BZCYYb anode, (f) $Ru_{0.75}Cu_{0.25}$-Ni/BZCYYb anode, (g) $Ru_{0.95}Cu_{0.05}$-Ni/BZCYYb anode, (h) Ru-Ni/BZCYYb anode in a symmetrical cell tested at 550-700 °C in NH_3; (i) Comparison of the R_p values for bare Ni/BZCYYb anode and Ru_xCu_{1-x}-Ni/BZCYYb anode in a symmetrical cell tested at 550-700 °C in NH_3.

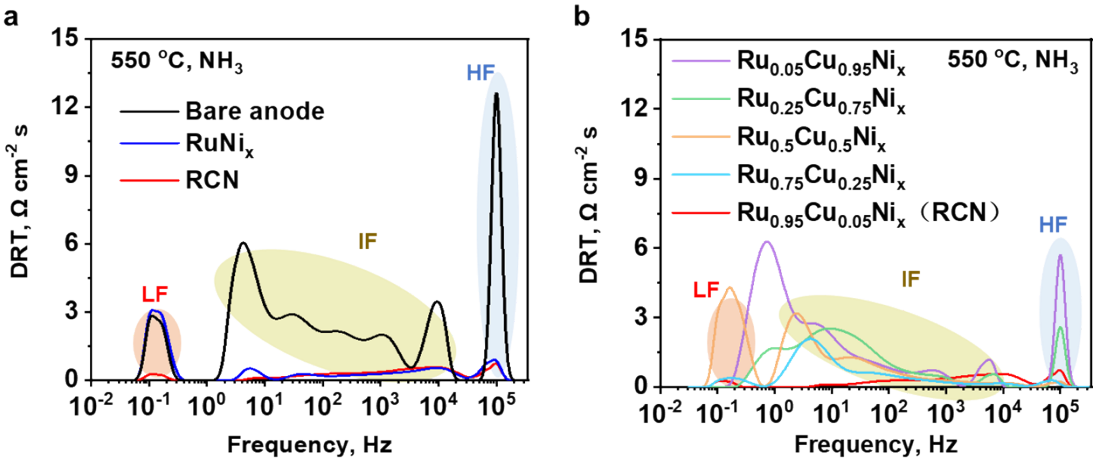

Figure S7. (a) DRT plots of the bare, $RuNi_x$, and RCN anodes in NH_3 at 550 °C; (b) DRT plots of the Ru_xCu_{1-x}-Ni/BZCYYb (x=0.05, 0.25, 0.5, 0.75, and 0.95) anodes in NH_3 at 550 °C.

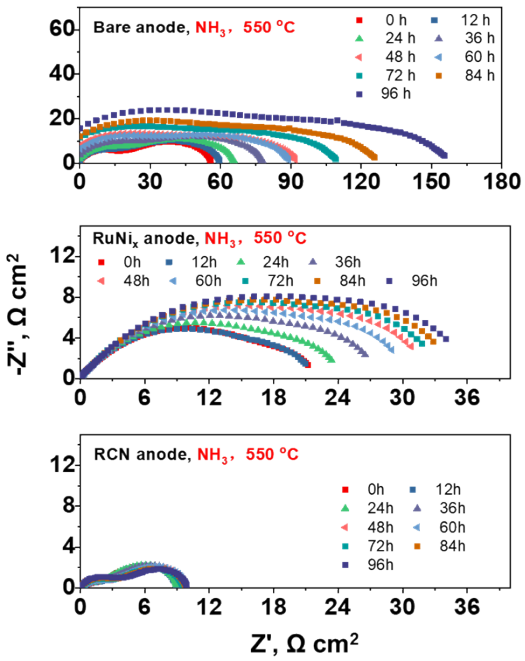

Figure S8. Electrochemical impedance spectra of the symmetrical anode cell with the bare, $RuNi_x$, and RCN anodes tested at 550 °C in NH_3 for 96 h.

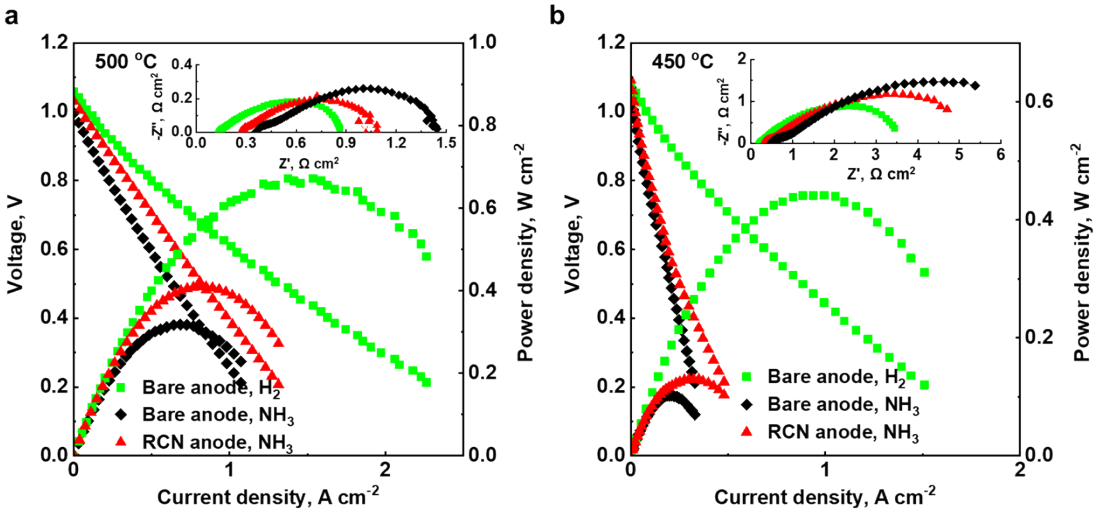

Figure S9. *IVP* curves and EIS of the PCFCs with a bare anode or a RCN anode fed by NH_3 or wet H_2 (a) at 500 °C, and (b) at 450 °C.

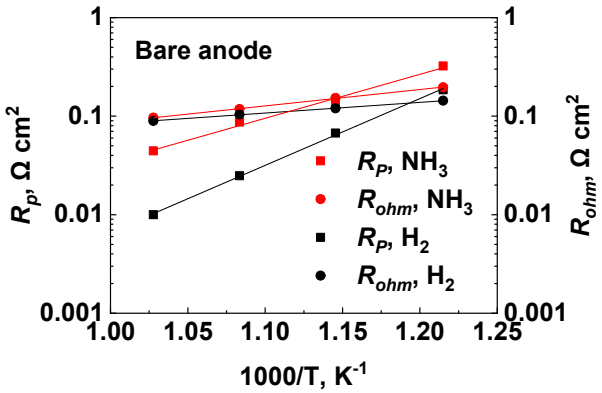

Figure S10. Arrhenius plot of the R_p and R_{ohm} for the cell with bare anode operated in wet H_2 or NH_3 at 550-700 ^oC.

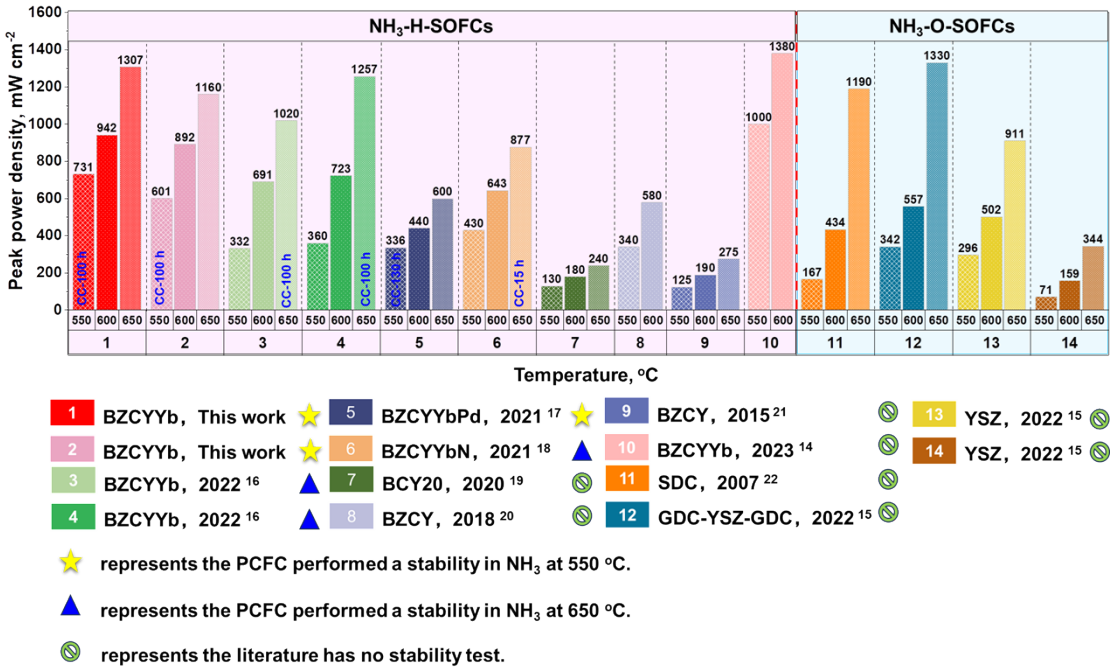

Figure S11. Comparison of P_{max} of state-of-the-art NH_3-SOFC at different temperatures. The details in Fig. S11 can be found in **Table S1** and **S2**, **ESI**†; The 550 °C-CC-100 h mean the SOFC performed a 1,00 h stability in NH_3 at 550 °C.

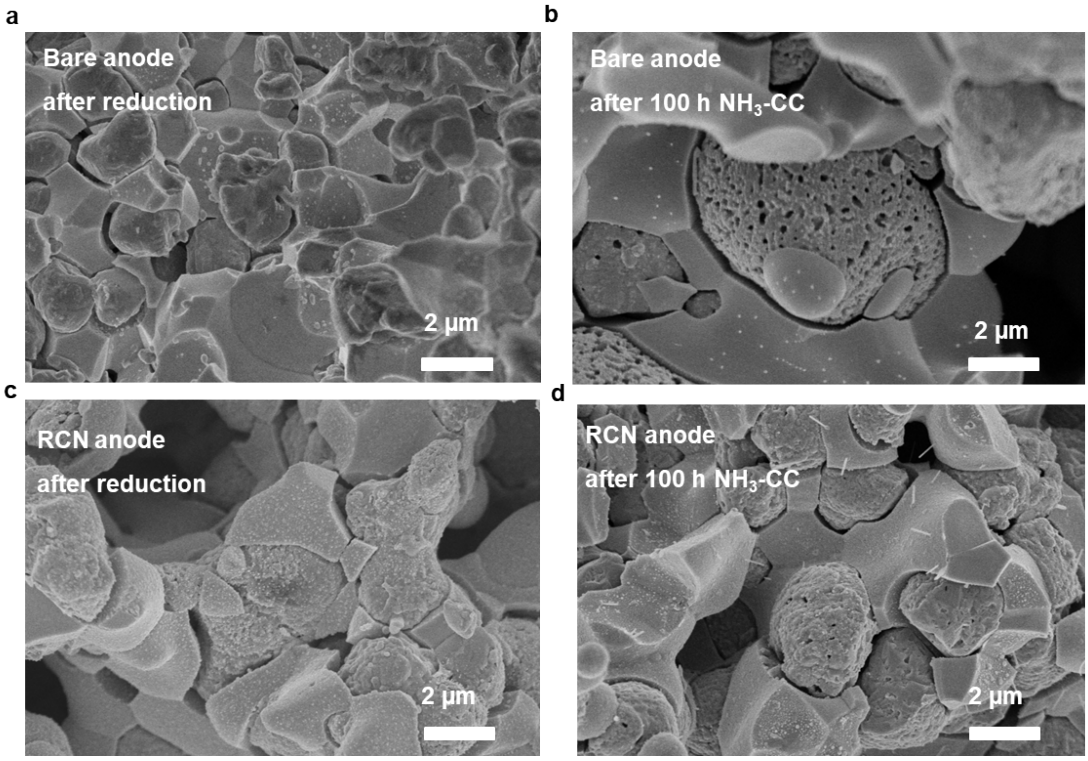

Figure S12. Cross-sectional SEM images of (a) bare anode after reduction in wet H_2; (b) bare anode after 100 h stability test in NH_3 at 550 °C; (c) RCN anode after reduction in wet H_2; and (d) RCN anode after 100 h stability test in NH_3 at 550 °C.

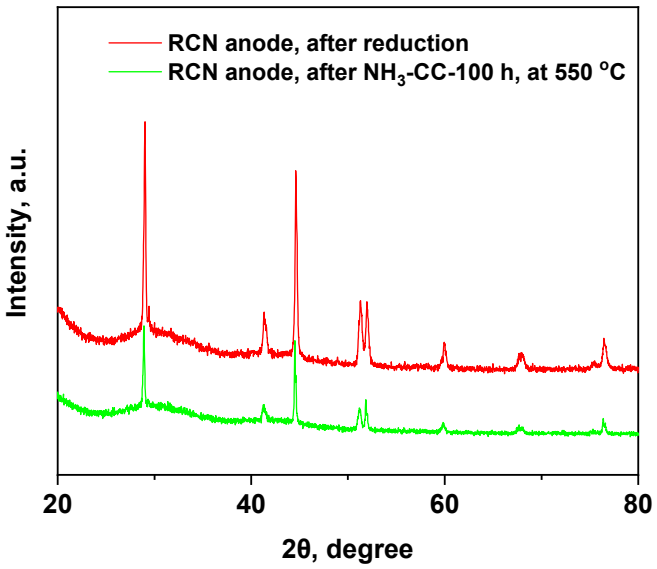

Figure S13. XRD patterns of the RCN anode after reduction on wet H_2 (red line), and after 100 h stability test in NH_3 at 550 °C (green line).

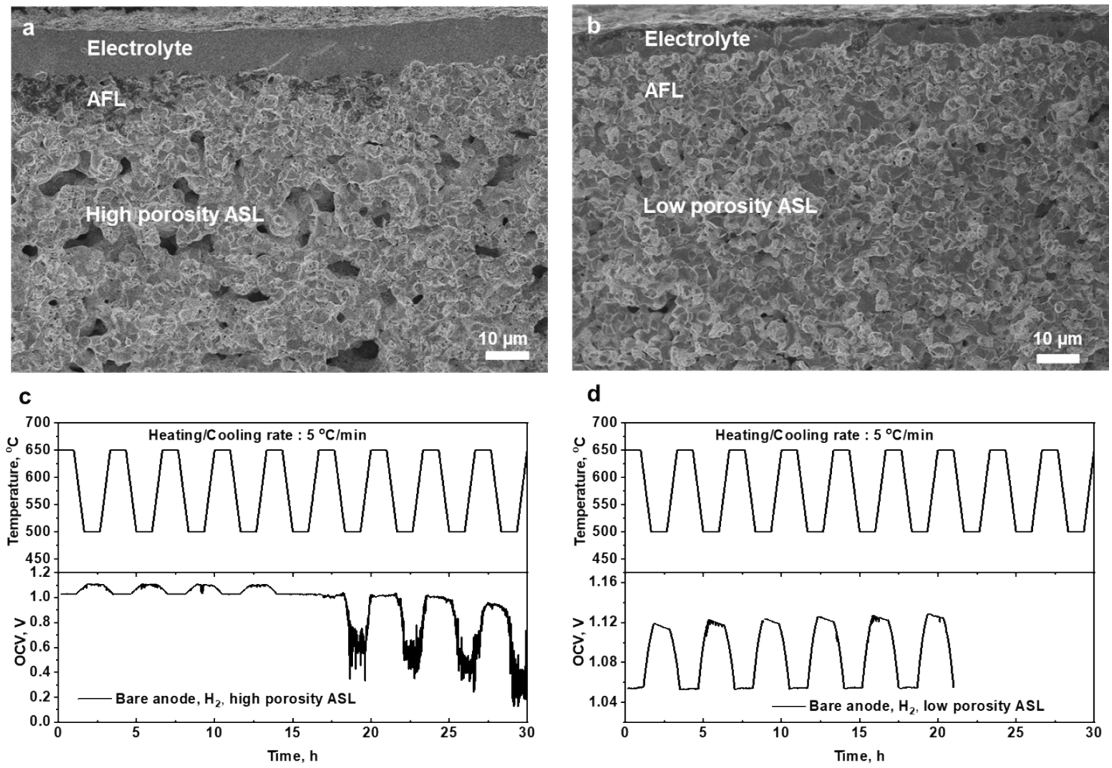

Figure S14. **Enhanced thermal cycling reliability of the PCFCs with low porosity ASL anode in H_2.** Typical SEM image of the (a) anode of the NH_3-PCFC with high porosity anode supporting layer (ASL) after reduction at 700°C in H_2 for 2 h, (b) the anode of the NH_3-PCFC with low porosity anode supporting layer (ASL) after reduction at 700°C in H_2 for 2 h. OCV of the single cells with (c) the anode with high porosity ASL, and (d) the anode with low porosity ASL fed with H_2 operated over thermal cycles ranging from 450 to 650 °C with rare heating/cooling rates of 5 °C/min. (In this study, we used a low porosity anode support layer (ASL) in PCFCs to offer adequate structural and mechanical strength. A cell with low porosity ASL has a more stable OCV during the thermal cycle than one with high porosity ASL.)

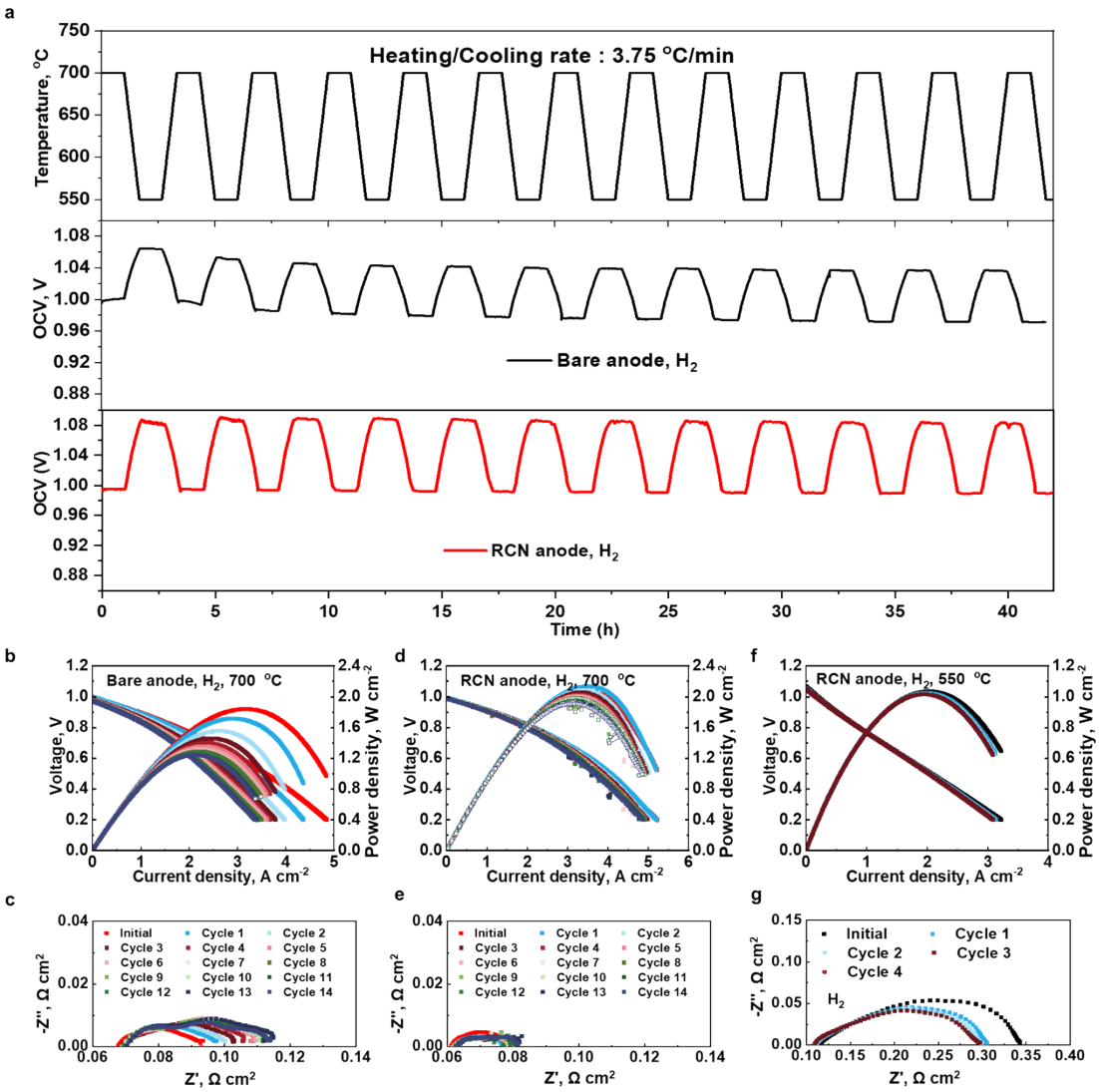

Figure S15. Enhanced thermal cycling reliability of the PCFCs with RCN anode in H_2. (a) OCV of the single cells with bare anode or RCN anode fed with H_2 operated over thermal cycles ranging from 550 to 700 °C with heating/cooling rates of 3.75 °C/min; (b) *IVP* curves, (c) EIS of the PCFCs with bare anode fed with H_2 at 700 °C after a different number of cycles; (d) *IVP* curves, (e) EIS of the single cell with RCN anode fed with H_2 at 700 °C after a different number of cycles; (f) *IVP* curves, (g) EIS of the single cell with RCN anode fed with H_2 at 550 °C after a different number of cycles.

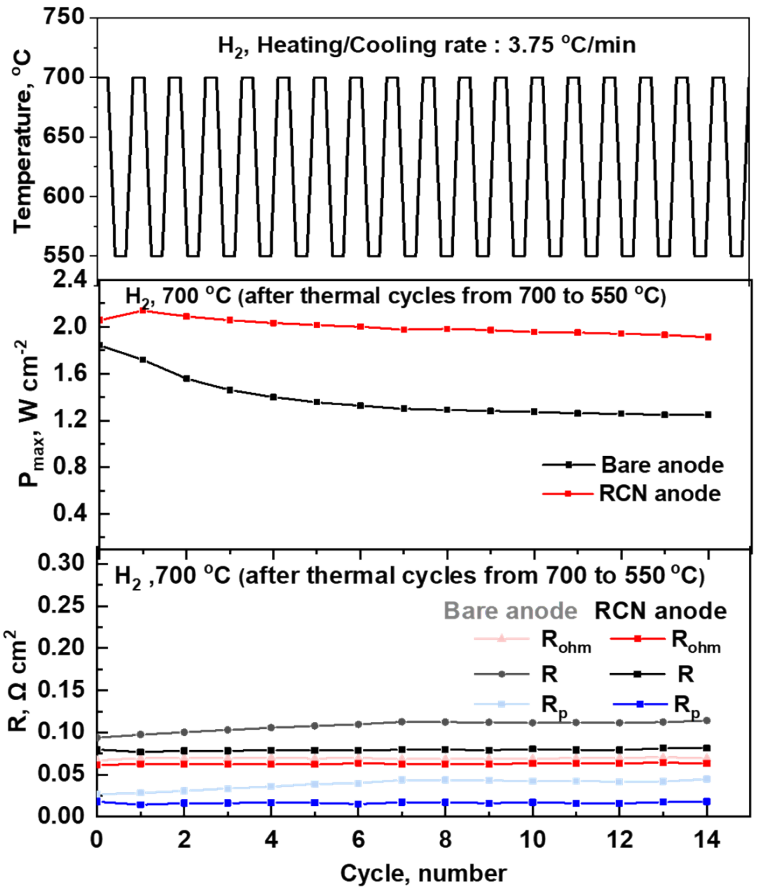

Figure S16. **Enhanced thermal cycling reliability of the PCFCs with RCN anode in H_2**. The P_{max}, and the R_p, R_{ohm} and R stability of the single cells with bare anode or RCN anode after a different number of cycles in H_2.

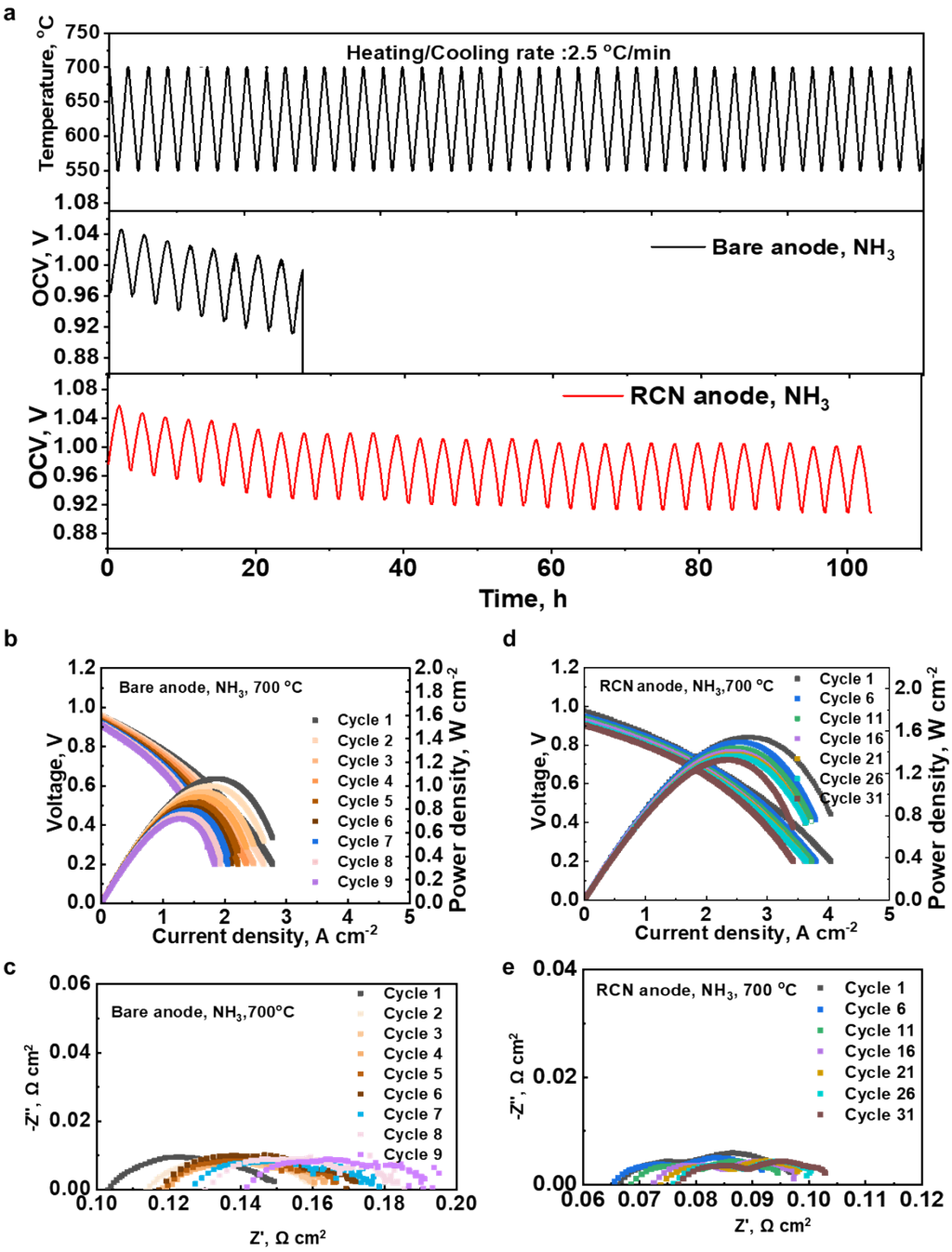

Figure S17. **Enhanced durability of the PCFCs with RCN anode in NH_3**. (a) OCV of the single cells with bare anode or RCN anode fed with NH_3 operated over thermal cycles ranging from 550 to 700 °C with heating/cooling rates of 2.5 °C/min. (b) *IVP* curves, (c) EIS of the single cell with bare anode fed with NH_3 at 700 °C after a different number of cycles; (d) *IVP* curves, (e) EIS of the single cell with RCN anode fed with NH_3 at 700 °C after a different number of cycles.

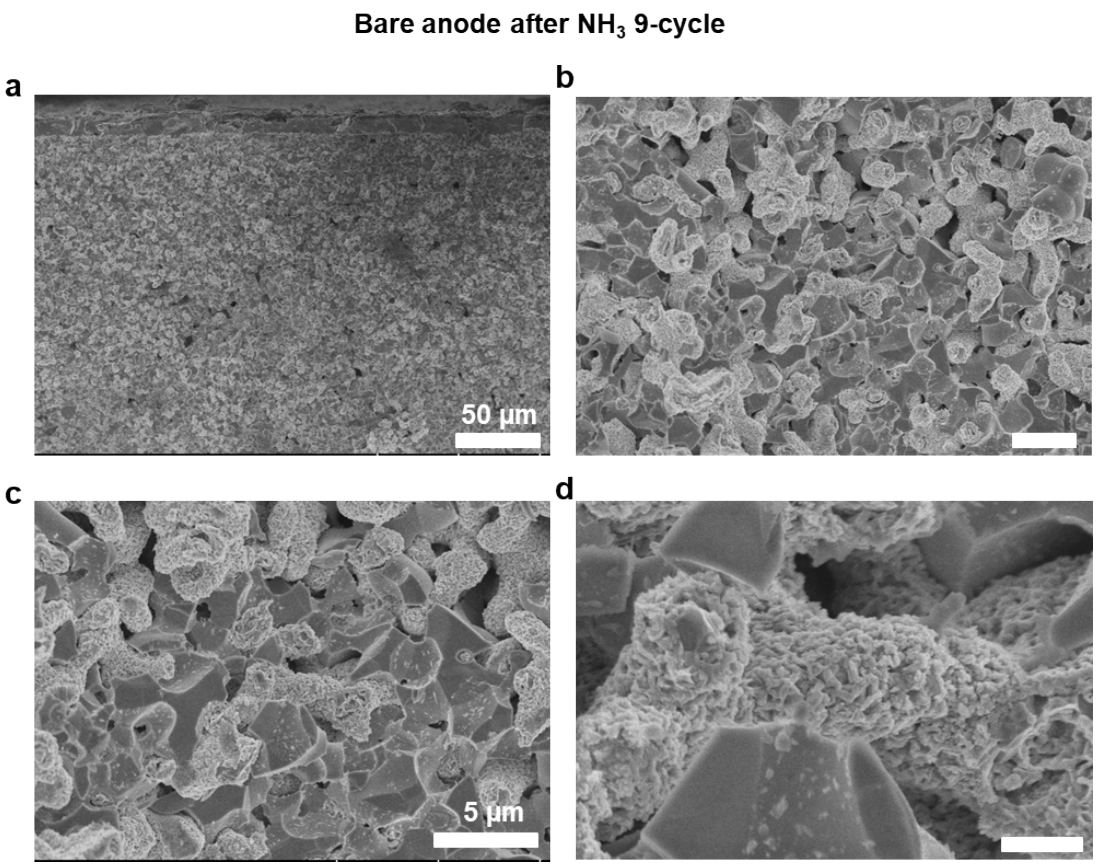

Figure S18. SEM images of the bare anode after a thermal cycles test between 550–700 °C under NH_3 fuel.

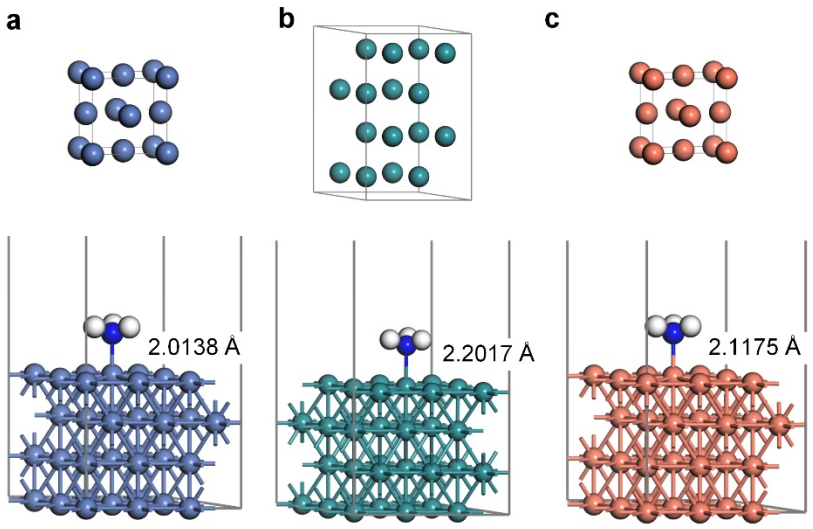

Figure S19. (a) Bulk models of Ni (a=b=c=3.5209 Å), Ru (a=b=2.7232 Å, c=4.3091 Å), and Cu (a=b=c= 3.6319 Å). (b) Representative configurations of NH_3 adsorption on N(111), Ru(0001), and Cu(111). The adsorption energies are summarized in **Supplementary Table S3**.

Supplementary Table

Table S1. Open circuit voltages and peak power densities of different ammonia-fed SOFCs at 550 °C based on changes in electrolyte thickness

Electrolyte	Cathode	Anode	Electrolyte thickness [μm]	Fuel	Temp. [°C]	OCV[V]	Cell performance [mW cm^{-2}]	Year[Ref]
BZCYYb	PBSCF	RuCu-Ni/BZCYYb	7	NH_3	550	1.049	732	This work
BZCYYb	PBSCF	Ni/BZCYYb	7	NH_3	550	1.024	601	This work
BZCYYb4411	$Ba_{0.62}Sr_{0.38}CoO_{3-\delta}$ - $Pr_{1.44}Ba_{0.11}Sr_{0.45}Co_{1.32}Fe_{0.68}O_{6-\delta}$	Ni/BZCYYb	3-4	NH_3	550	1.07	1000	2023[14]
GDC-YSZ-GDC	LSC	TF-Ni-GDC	650-300-150 nm	NH_3	550	1.09	342	2022[15]
YSZ	LSC	TF-Ni-YSZ	1	NH_3	550	1.07	296	2022[15]
YSZ	LSCF-GDC	Bulk-Ni-YSZ	6	NH_3	550	1.22	71	2022[15]
BZCYYb	PBSCF	Ni/BZCYYb	10	NH_3	550	1.015	332	2022[16]
BZCYYb	PBSCF	Ni-Fe/BZCYYb	10	NH_3	550	1.034	360	2022[16]
BZCYYbPd	BCFZY	Ni-BZCYYbPd	20	NH_3	550	1.1	336	2021[17]
BZCYYbN	BCFZY	Ni-BZCYY	4	NH_3	550	1.09	430	2021[18]
BCY20	BCY20-LSCF	Ni-BCZY	50-60	NH_3	550	1.12	130	2020[19]
BZCY	$La_{0.6}Sr_{0.4}Co_{0.2}Fe_{0.8}O_{3-d}$ (LSCF)	Pd	1	NH_3	550	1	340	2018[20]
$BaZr_{0.1}Ce_{0.7}Y_{0.2}O_{3-\delta}$ (BZCY)	$Ba_{0.5}Sr_{0.5}Co_{0.8}Fe_{0.2}O_{3-\delta}$ (BSCF)	Ni-BZCY	35	NH_3	550	0.98	125	2015[21]
SDC	$Ba_{0.5}Sr_{0.5}Co_{0.8}Fe_{0.2}O_{3-\delta}$(BSCF)	NiO-SDC	10	NH_3	550	0.795	167	2007[22]

Table S2. A list of studies that have reported NH_3 long-term operation of PCFC.

Cell structure/sample details	Temperature/duration	Fuel composition	Performance/current density	Remarks	Year[Ref]
platinum ink A-4338|BCGP| platinum ink A-4338	700 °C/96 h	NH_3	~36 mW cm^{-2}	no detectable degradation	2005 [23]
monolithic BCE fuel cell: $BaCe_{0.85}Eu_{0.15}O_3$, BCE electrolyte. Engelhard platinum ink A-4338 for the anode and cathode.	700 °C/200 h	NH_3	~30 mW cm^2	no detectable decay in performance	2006 [24]
NiO–BCE|BCGP|Pt	600 °C/500 h	NH_3	48 mW at 100 mA	little degradation	2008 [25]
Ni-BZCYYbPd|BZCYYbPd|BCFYZ	550 °C /130h	NH_3	~0.76 V at a current density of 200 mA cm^2	dropped by only 0.01 V after 130 h	2021[17]
~500 μm Ni-BCZYYb/ ~4 μm BCZYYbN ($BaCe_{0.7}Zr_{0.1}Y_{0.1}Yb_{0.1}Ni_{0.04}O3-\delta$)/ a ~20 μm BCFZY ($BaCo0.4Fe_{0.4}Zr_{0.1}Y_{0.1}O_{3-\delta}$)	650 °C /15h	NH_3	~0.78 V at a current density of 500 mA cm^2	the voltage dropped to zero	2021
Ni-BZCYYb|BZCYYb|PBSCF	650 °C /100h	NH_3	~0.9 V at a current density of 500 mA cm^2	0.0008 V h^{-1}	2022 [16]
NiFe-BZCYYb|BZCYYb|PBSCF	650 °C /100h	NH_3	~0.9 V at a current density of 500 mA cm^2	0.00022 V h^{-1}	2022 [16]
Ni-BZCYYb|BZCYYb|PBSCF (tubular cell)	650 °C /4h	NH_3	~0.749 V at 0.5 A cm^{-2}	the voltage dropped to zero	2022 [26]

Fe|Ni-BZCYYb|BZCYYb|PBSCF (tubular cell)	650 °C /20h	NH_3	~0.8 V at 0.5 A cm^{-2}	the voltage dropped by 0.1 V	2022 [26]
Ni-BZCYYb|BZCYYb|PBSCF	550 °C /100h	NH_3	~0.9 V at a current density of 200 mA cm^2	0.095 V per 100 h	This work
RuCuNi-BZCYYb|BZCYYb|PBSCF	550 °C /100h	NH_3	~0.94 V at a current density of 200 mA cm^2	0.016 V per 100 h	This work

Table S3. Compilation of adsorption energies (eV) of surface species on Ni(111), Ru(0001), Cu(111), and RuCuNi(111).

	Ni(111) [1]	Ru(0001)	Cu(111)	RuCuNi(111)
NH_3*	–0.68, atop	–0.89 atop	–0.43 atop	–0.63 [2] atop
E_a : NH_3* + * = NH_2* + H*	1.40	1.51	1.94	-
N*	–5.27 fcc	–5.62 fcc	–3.52 fcc	–5.15 [2] fcc, hcp
H*	–2.79 fcc	–2.88 fcc	–2.47 fcc	–2.75 [2] fcc, hcp
E_a : 2N* = N_2(g) + 2*	1.84	-	-	1.67
ΔE: 2N* = N_2(g) + 2*	0.17	-	-	0.19

1. Reference: Pan, Y. et al., A high-performance and durable direct NH_3 tubular protonic ceramic fuel cell integrated with an internal catalyst layer, *Applied Catalysis B: Environmental*, 306, 121071 (2022).
2. Averaged values. E_a and ΔE are a reaction barrier and reaction energy.

References

1. G. Kresse and J. Hafner, *Phys. Rev. B*, 1993, **47**, 558-561.
2. G. Kresse and J. Furthmuller, *Phys. Rev. B*, 1996, **54**, 11169-11186.
3. J. P. Perdew, K. Burke and M. Ernzerhof, *Phys. Rev. Lett.*, 1996, **77**, 3865-3868.
4. G. Kresse and D. Joubert, *Phys. Rev. B*, 1999, **59**, 1758-1775.
5. G. Henkelman, B. P. Uberuaga and H. Jónsson, *J. Chem. Phys.*, 2000, **113**, 9901-9904.
6. P. Jing, M. Liu, Y. Pu, Y. Cui, Z. Wang, J. Wang and Q. Liu, *Sci Rep*, 2016, **6**, 37701.
7. H. Sun, R. Tang, X. Zhang, S. Zou, Y. Shi, K. Chen, S. Sarina and J. Huang, *Carbon Capture Science & Technology*, 2023, **6**, 100100.
8. C. Wang, J. Bai, H. Wang, Y. Li, Y. Li, F. Liu, X. Liang, P. Sun and G. Lu, *Sensor Actuat B-Chem*, 2022, **351**, 130900.
9. Y. Zhang, Y. Chen and F. Chen, *J. Power Sources*, 2015, **277**, 277-285.
10. X. Mao, J. Sang, C. Xi, Z. Liu, J. Yang, W. Guan, J. Wang, C. Xia and S. C. Singhal, *Int. J. Hydrogen Energy*, 2022, **47**, 23324-23334.
11. S. Primdahl and M. Mogensen, *J. Electrochem. Soc.*, 1998, **145**, 2431.
12. S. Primdahl and M. Mogensen, *J. Electrochem. Soc.*, 1999, **146**, 2827.
13. D. Zeng, M. Wu, M. Yousaf, H. Song, Z. Wan, X. Gao, J. Shao and Y. Tao, *J. Power Sources*, 2024, **592**, 233939.
14. F. Liu, H. Deng, D. Diercks, P. Kumar, M. H. A. Jabbar, C. Gumeci, Y. Furuya, N. Dale, T. Oku, M. Usuda, P. Kazempoor, L. Fang, D. Chen, B. Liu and C. Duan, *Nat Energy*, 2023, **8**, 1145-1157.
15. S. Oh, M. J. Oh, J. Hong, K. J. Yoon, H.-I. Ji, J.-H. Lee, H. Kang, J.-W. Son and S. Yang, *Iscience*, 2022, **25**, 105009.
16. H. Zhang, Y. C. Zhou, K. Pei, Y. X. Pan, K. Xu, Y. Ding, B. T. Zhao, K. Sasaki, Y. M. Choi, Y. Chen and M. L. Liu, *Energ Environ Sci*, 2022, **15**, 287-295.
17. F. He, Q. Gao, Z. Liu, M. Yang, R. Ran, G. Yang, W. Wang, W. Zhou and Z. Shao, *Adv. Energy Mater.*, 2021, **11**, 2003916.
18. L. Zhu, C. A. Cadigan, C. Duan, J. Huang, L. Bian, L. Q. Le, C. H. Hernandez, V. Avance, R. O'Hayre and N. P. Sullivan, *Commun Chem*, 2021, **4**, 1-10.
19. K. Miyazaki, H. Muroyama, T. Matsui and K. Eguchi, *Sustain Energ Fuels*, 2020, **4**, 5238-5246.
20. Y. Aoki, T. Yamaguchi, S. Kobayashi, D. Kowalski, C. Zhu and H. Habazaki, *Glob Chall*, 2018, **2**, 1700088.
21. J., Yang, T., Akagi, T., Okanishi, H., Muroyama, T. and Matsui, *Fuel Cells*, 2015, **15**, 390-397.
22. G. Y. Meng, C. R. Jiang, J. J. Ma, Q. L. Ma and X. Q. Liu, *J Power Sources*, 2007, **173**, 189-193.
23. N. Maffei, L. Pelletier, J. P. Charland and A. McFarlan, *J Power Sources*, 2005, **140**, 264-267.
24. N. Maffei, L. Pelletier, J. P. Charland and A. McFarlan, *J Power Sources*, 2006, **162**, 165-167.
25. N. Maffei, L. Pelletier and A. McFarlan, *J Power Sources*, 2008, **175**, 221-225.

26. Y. Pan, H. Zhang, K. Xu, Y. Zhou, B. Zhao, W. Yuan, K. Sasaki, Y. Choi, Y. Chen and M. Liu, *Appl Catal B-Environ*, 2022, **306**, 121071.